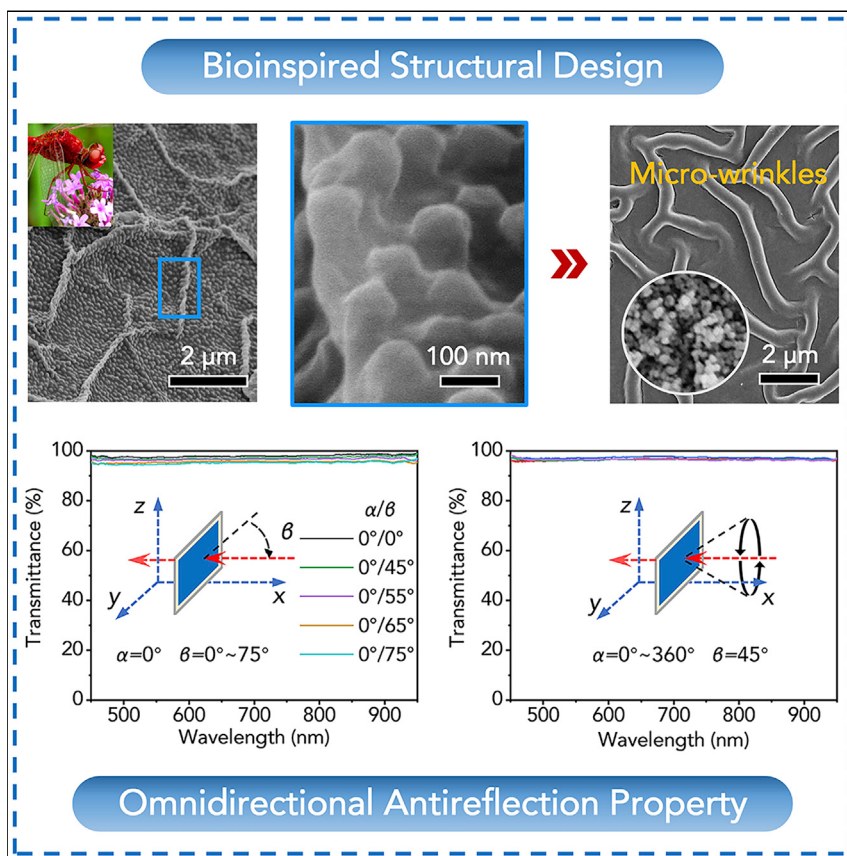


## Article

# Bioinspired omnidirectional antireflective film with mechanical durability for efficient solar energy collection



Reducing reflectivity and maximizing the absorption of light are the prime goals for efficient photoelectric conversion in solar cells, anti-glare in sophisticated optical instruments, and video stealth technology. Therefore, developing omnidirectional antireflection materials to break the angle-dependent limit and boost antireflection efficiency is of great significance. This work reveals the underlying omnidirectional antireflection mechanism of the dragonfly ommatidium and reports a biomimetic omnidirectional antireflective film, benefiting efficient solar energy harvesting and related practical applications.



## Development

Practical, real world, technological considerations and constraints

Hanliang Ding, Bo Li, Ze Wang,  
Shichao Niu, Zhiwu Han, Luquan  
Ren

boli@jlu.edu.cn (B.L.)  
niushichao@jlu.edu.cn (S.N.)

### Highlights

The internal structure of the dragonfly ommatidium exhibits omnidirectional antireflection

Equisite biomimetic structures could be prepared via a self-assembly strategy

Biomimetic antireflective film enables efficient omnidirectional antireflection

Biomimetic structure is the key to boosting the photovoltaic performance of solar cells

## Article

# Bioinspired omnidirectional antireflective film with mechanical durability for efficient solar energy collection

Hanliang Ding,<sup>1</sup> Bo Li,<sup>1,2,\*</sup> Ze Wang,<sup>1,2</sup> Shichao Niu,<sup>1,3,\*</sup> Zhiwu Han,<sup>1</sup> and Luquan Ren<sup>1,2</sup>

## SUMMARY

Soaring developments in solar cells raise an urgent demand for superior antireflective (AR) materials to tackle the concern of their inadequate photovoltaic efficiency. Unfortunately, conventional AR films still suffer from a deficiency in omnidirectional antireflection and mechanical durability, significantly weakening their light-harvesting capability. Herein, a scalable biomimetic antireflective film (BARF) with ommateum-inspired multiscale hierarchical architecture was prepared using a method combining layer-by-layer thermal decomposition and *in situ* self-assembly. Remarkably, the BARF exhibited a transmittance of over 95% in light incident angles from  $-75^\circ$  to  $75^\circ$ . Thereby, the output voltage of solar cells coated with BARF increased by 30.48% compared with commercial AR film. Furthermore, the BARF demonstrated excellent mechanical durability in falling-sand tests ( $\sim 2\%$  transmittance loss). This work offers a general strategy for mass production of omnidirectional and durable AR films that are suitable for practical applications of protective AR film in solar cells, light pollution treatment, and video stealth technology.

## INTRODUCTION

Reducing reflectivity and maximizing the absorption of light are the prime goals for efficient photoelectric conversion in solar cells,<sup>1–7</sup> anti-glare in sophisticated optical instruments, and video stealth technology.<sup>8,9</sup> However, conventional light-manipulation technologies are limited by the barely adequate antireflective ability in restricted light incident angles and the relatively narrow spectral region,<sup>10–14</sup> which results in inefficient light management. Fortunately, living organisms could provide ingenious enlightenment to help overcome the above-mentioned challenges.<sup>14–19</sup> After billions of years of evolution, creatures have experimented with various solutions to their survival challenges and have improved on the successful ones, which could provide ready answers to scientific and technical problems and inspire us with a series of novel designs. Abundant species in nature have been investigated and mimicked for many years, with the aim to design unique structured materials with excellent optical features and extensive practical values, such as leaf-inspired antireflective materials,<sup>15</sup> high-transmission surfaces mimicking cicada wings,<sup>16</sup> light-trapping films inspired by butterfly wings, and so on.<sup>20</sup> To a certain extent, the above-mentioned biomimetic surfaces have relieved the limitations to efficient antireflection (AR) of light in the broadband spectral region.<sup>14,21</sup> However, despite acceptable AR efficiencies, there are still several drawbacks to existing light-management materials, such as angle-dependent light harvesting,<sup>22</sup> poor mechanical durability,<sup>23–27</sup> small-scale production,<sup>28–31</sup> and performance mismatch between multiple materials.<sup>32–34</sup>

## PROGRESS AND POTENTIAL

Antireflective film usually plays a crucial role in the enhancement of light management, which accounts for its extremely extensive applications in solar cells, sophisticated optical instruments, and video stealth devices. Conventional antireflective films, however, still suffer from a deficiency in omnidirectional antireflection and mechanical durability, significantly weakening their performance in practical applications. Here, we propose a scalable biomimetic antireflective film with omnidirectional antireflection and mechanical durability, benefiting from ommateum-inspired hierarchical architectures. This work reveals the omnidirectional antireflective mechanism of the sophisticated structure inside the dragonfly ommateum. Moreover, the findings in this work offer a general and economical yet effective methodology for creating high-performance multifunctional films with omnidirectional antireflection and mechanical durability for broad practical applications.

Regarding omnidirectional AR properties, in order to prey and to avoid predators without blind spots, dragonflies have evolved compound eyes with an omnidirectional view and stable collection of optical information.<sup>35–38</sup> For compound eyes, the surface structure is typically made up of abundant two-dimensional (2D) hexagonal microstructures with non-close-packed tapered nanopillars. The irregularly aligned nanopillars suppress the surface reflection of obliquely incident light and transmit complete optical information to the photoreceptor cells. In addition, nanostructures with smaller lateral dimensions than the light wavelength could diminish the Fresnel surface reflection loss in a relatively wide wavelength region and at incident angles. Consequently, since compound eyes have great potential in omnidirectional and broadband AR performance, antireflective functional materials mimicking compound eyes have recently been extensively investigated. However, existing research mainly focuses on the AR performance of the 2D surface structure, ignoring the internal 3D structures that possess a more intimate and elaborate interaction with light. Accordingly, the internal exquisite structures and the underlying superior AR mechanism have not been revealed so far.

As for the preparation of biomimetic antireflective film (BARF), the self-assembly method is a feasible candidate,<sup>39–41</sup> not only because of its economical and high-efficiency features, but, more importantly, for the ability to precisely construct biomimetic structures. However, due to the difficulty in maintaining the uniformity and stability of reactants and reaction processes in a large space, conventional self-assembly methods cannot achieve the flawless and large-scale production of exquisite biomimetic structures. Fortunately, utilizing the spin-coating process,<sup>42–44</sup> liquid reactants could be evenly and extensively coated on a substrate. Subsequently, by combining the layer-by-layer thermal decomposition and self-assembly processes, structural defects such as agglomeration and voids could be avoided to the greatest extent.<sup>45–47</sup> Furthermore, the close-packed arrangement of particles and the single-component feature could endow BARFs with enhanced mechanical durability.

In this work, a BARF with 3D hierarchical optical structures was successfully fabricated through layer-by-layer thermal decomposition of zinc acetate sol and *in situ* self-assembly of non-toxic ZnO nanospheres.<sup>48–50</sup> When a BARF was applied to glass and silicon substrates, the assembly possessed superior omnidirectional antireflective properties, which was demonstrated through angle-resolved spectrometry. Remarkably, the BARF exhibited a transmittance of over 95% in light incident angles from  $-75^\circ$  to  $75^\circ$ . In addition, the durability of the BARF was illustrated by scratching and falling-sand tests. The BARF demonstrated excellent mechanical durability through a falling-sand test ( $\sim 2\%$  transmittance loss). In fact, the single-component feature of the BARF dealt with the dilemma of poor mechanical strength caused by an unstable connection between heterogeneous materials. At the same time, the close-packed arrangement of ZnO nanospheres further enhanced the wearproof properties of the BARF. What is more, it is worth pointing out that the BARF also exhibited excellent anti-glare performance, which provided more possibilities for its practical application in the near future.

## RESULTS AND DISCUSSION

### Structural features and antireflective property of the dragonfly ommateum

To investigate the surface morphology and internal structure of the red dragonfly (*Crocothemis servilia*) ommateum from macro to micro, an ultra-depth-of-field microscope and a scanning electron microscope (SEM) were used to observe its hexagonal microstructures on the cornea and nanostructures under the cornea. As for

<sup>1</sup>Key Laboratory of Bionic Engineering, Ministry of Education, Jilin University, Changchun, Jilin 130022, China

<sup>2</sup>School of Mechanical and Aerospace Engineering, Jilin University, Changchun, Jilin 130022, China

<sup>3</sup>Lead contact

\*Correspondence: [boli@jlu.edu.cn](mailto:boli@jlu.edu.cn) (B.L.), [niushichao@jlu.edu.cn](mailto:niushichao@jlu.edu.cn) (S.N.)

<https://doi.org/10.1016/j.matt.2022.06.015>

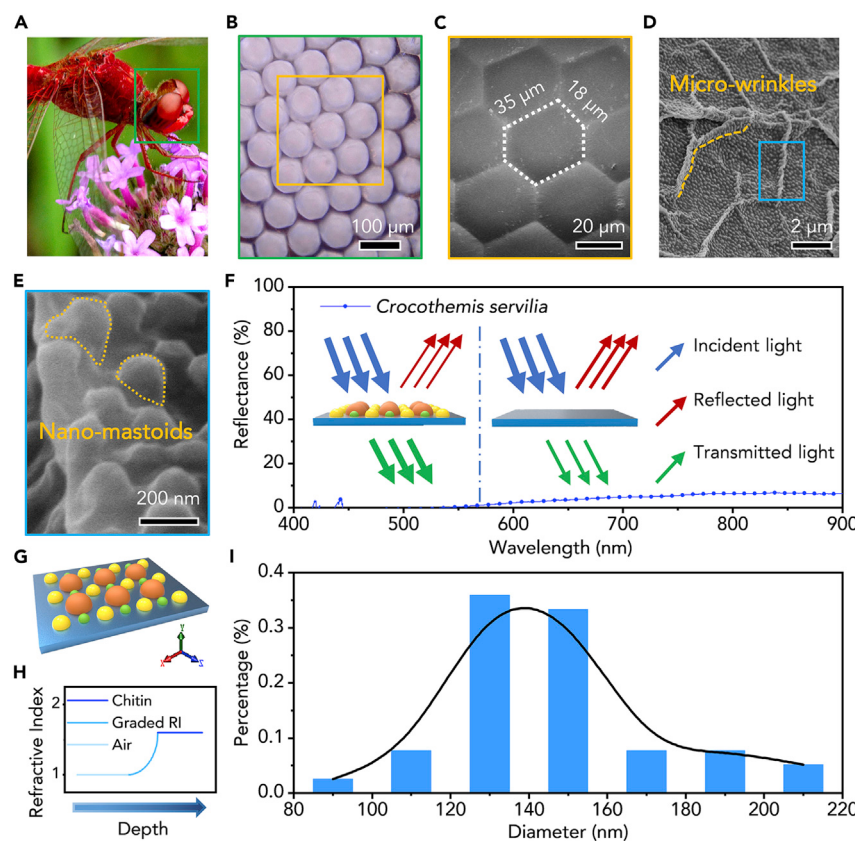


**Figure 1. Dragonfly *Crocothemis servilia* and reflectance spectrum of compound eyes**

- (A and B) Digital pictures of a dragonfly and its compound eye.  
(C) SEM image of 2D hexagonal structures on the compound eye surface.  
(D and E) SEM images of delicate 3D structures (microscale wrinkles and nanoscale mastoids) inside the compound eyes.  
(F) Reflectance spectrum of dragonfly compound eyes. The inset demonstrates the antireflective function of nanoscale mastoid structures.  
(G) Simplified structural model of the nanoscale mastoid array. The size distribution of the nanoscale mastoids is consistent with the Gaussian distribution.  
(H) Simplified structural model features a gradient refractive index from air to compound eye surface, which could weaken the Fresnel reflection.  
(I) Size distribution of nanoscale mastoids on microscale wrinkles.

the optical properties of the ommatuum, a spectrometer was applied to measure its reflectance.

As shown in Figure 1A, the red dragonfly has two eyes with a large surface area, which take up a major part of the head. The detailed enlarged image in Figure 1B shows that there is a layer of abundant 2D hexagonal arrays on the ommatuum surface. The compound eye surface is in a non-planar state; the reflected light appears red on most of the surface, while the edges appear as light blue fluorescence. The side lengths of one non-regular hexagonal structure are measured in Figure 1C.

Conventional AR strategies mainly focus on the 2D feature structures (array mode and characteristic morphology) on the compound eye surface, ignoring the AR characteristics of the internal 3D structures, which possess a more exquisite architecture and elaborate interaction with light. Therefore, we paid more attention to the feature structures inside the compound eye. The compound eye was broken up into pieces

and examined carefully. From SEM images in [Figures 1D](#) and [1E](#), it could be found that the wrinkle structures with nanomastoids extended all over the surface of the biological tissue. The mastoids on wrinkles were randomly distributed but very dense. There were about 60 papillae in  $1\text{ }\mu\text{m}^2$ . It could be seen that all mastoids were hemispherical, as shown in [Figure 1E](#). The model in [Figure 1G](#) roughly shows the size proportion of the mastoid structures, which were distinguished by different colors. Their diameters were symmetrically distributed from 80 to 220 nm with a center size of 140 nm ([Figure 1I](#)).

The reflectance of the ommateum from 400 to 900 was measured through a spectrophotograph and is shown in [Figure 1F](#). It was found that the reflectance in the visible range was less than 5%. More important, the reflectance was close to 0% in the short-wave range. This low reflectivity proved that the compound eyes of the dragonfly *C. servilia* possess excellent AR properties. The nanomastoids mentioned above and the surrounding air form a graded refractive index (GI) around the ommateum surface, which breaks the abrupt change in refractive index (RI) from the heterogeneous interfaces. The GI allows the light to change direction gradually as it is propagated, thereby weakening the Fresnel surface reflection in a continuous medium. As shown in [Figure 1H](#), the GI increased slowly from 1 for air to 1.6 for chitin. The model of light passing through the surface with the mastoid structure is shown in [Figure 1F](#).

#### Fabrication and characterization of BARF

[Figure 2A](#) shows the fabrication process of the bioinspired ZnO antireflective film.  $\text{Zn}(\text{CH}_3\text{COOH})_2$  was decomposed at a high temperature to form ZnO, acetone, and  $\text{CO}_2$ . At the same time, acetone was heated into a gaseous state that escapes from the BARF with  $\text{CO}_2$ . The preparation process mainly comprises five steps: cleaning the substrate, preparing the sol-gel solution, spin-coating the film, a pre-heating treatment, and an annealing treatment. More detailed information is given in the [experimental procedures](#).

During fabrication, the three crucial factors that affected the optical properties of BARF were the spin-coating time, annealing temperature, and spin-coating speed. The annealing temperature started at  $330^\circ\text{C}$  and was increased by  $20^\circ\text{C}$  each time to  $390^\circ\text{C}$ . The spin-coating speed was increased from 1,600 to 2,600 r/min, at increments of 200 r/min.

[Figures 2B–2G](#) show the surface topography of BARF at different fabrication temperatures. [Figures 2B–2D](#) were photographed at low magnification, while [Figures 2E–2G](#) show the surface structure at higher magnification. As can be seen from [Figures 2B–2D](#), the density of the surface wrinkles became higher and higher with the increase in temperature. [Figures 2E–2G](#) show more detailed information on the wrinkles in the BARF. The ZnO molecule decomposed during the heating process and gradually agglutinated into nanospheres. Then the nanospheres were stacked *in situ* layer by layer automatically on the substrate surface to construct a close-packed bottom part of the BARF. However, the surface nanospheres were wrinkled due to thermal motion under high temperatures. When the sol liquid on the surface evaporated, a tight binding force was formed among the nanospheres. Due to the randomness of thermal motion and volatilization of the sol, the growth of the wrinkles on the BARF was in a state of disorder. And the width of the wrinkles was also changing along with the growth of the wrinkles ([Figures 2H](#) and [2I](#)). This randomness of distribution echoed the random wrinkles on the ommateum, which showed nearly 97% transmittance in the wavelength range of 500–900 nm. For another vital

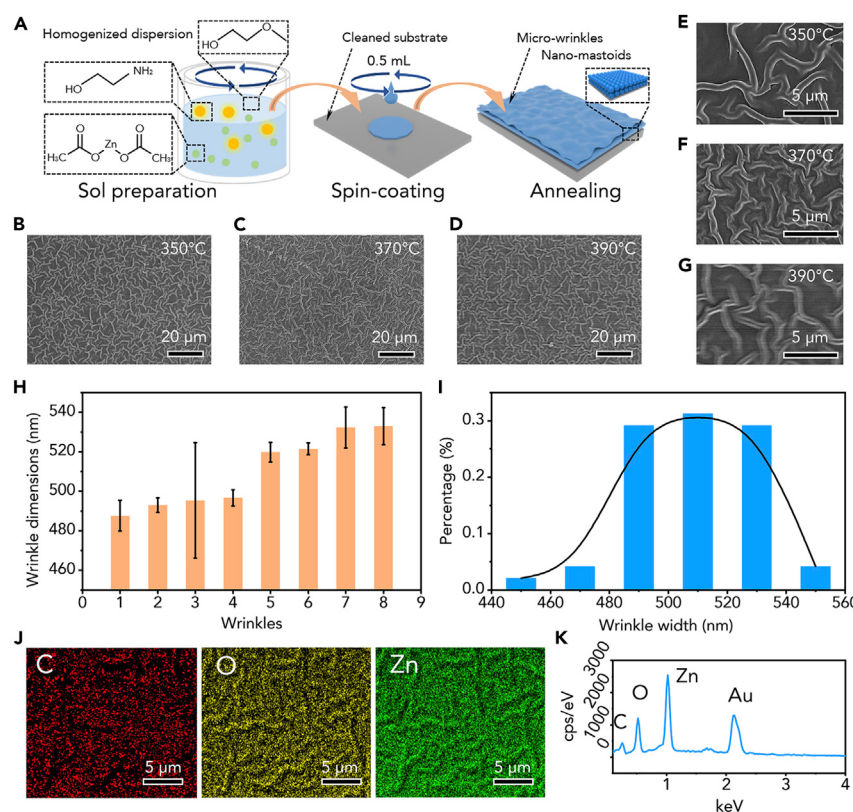


**Figure 2. Basic characterization of BARF**

- (A) Schematic of the fabrication process for BARF.  
(B–D) Surface textures of BARFs prepared at 350°C, 370°C, and 390°C. As the temperature rises, the density of the wrinkle structures is gradually enhanced.  
(E–G) Enlarged SEM images of the shapes and distribution of irregular wrinkles distributed on BARFs prepared at 350°C, 370°C, and 390°C.  
(H and I) Statistical analysis of the wrinkle sizes of BARF prepared at 370°C.  
(J) Elemental mapping images of Zn, O, and C in the BARF prepared at 370°C.  
(K) EDS spectrum of BARF prepared at 370°C.

factor, as the spin speed increased, the coating thickness became thinner and thinner as the centrifugal force increased. When the surface tension was not able to withstand the tear of centrifugal force, the BARF surface became incomplete and uneven in thickness, which affected the integral optical performance. [Figure S1](#) shows the surface morphology of the BARF at different spinning speeds under 370°C. As can be seen from the images, the BARFs of the three rotation coating speeds had similar surface structures. The wrinkle density and plane area on the surfaces had similar sizes, which indicated that the spin-coating speed did not affect the surface morphology.

In addition, to find out whether the glass substrate was completely covered with BARF, energy-dispersive spectrometry (EDS) was carried out on the BARF to analyze its surface composition from chemical elements. [Figure 2J](#) shows the distribution of the three elements on the BARF surface, and [Figure 2K](#) shows the contents of the three chemical elements (more information is presented in [Figure S2](#)). As can be seen from the figures, the three elements on the coating were evenly distributed, and the surface was mainly composed of oxygen and zinc, which indicated that ZnO nanoparticles were successfully prepared in the process of synthesis and thermal decomposition.

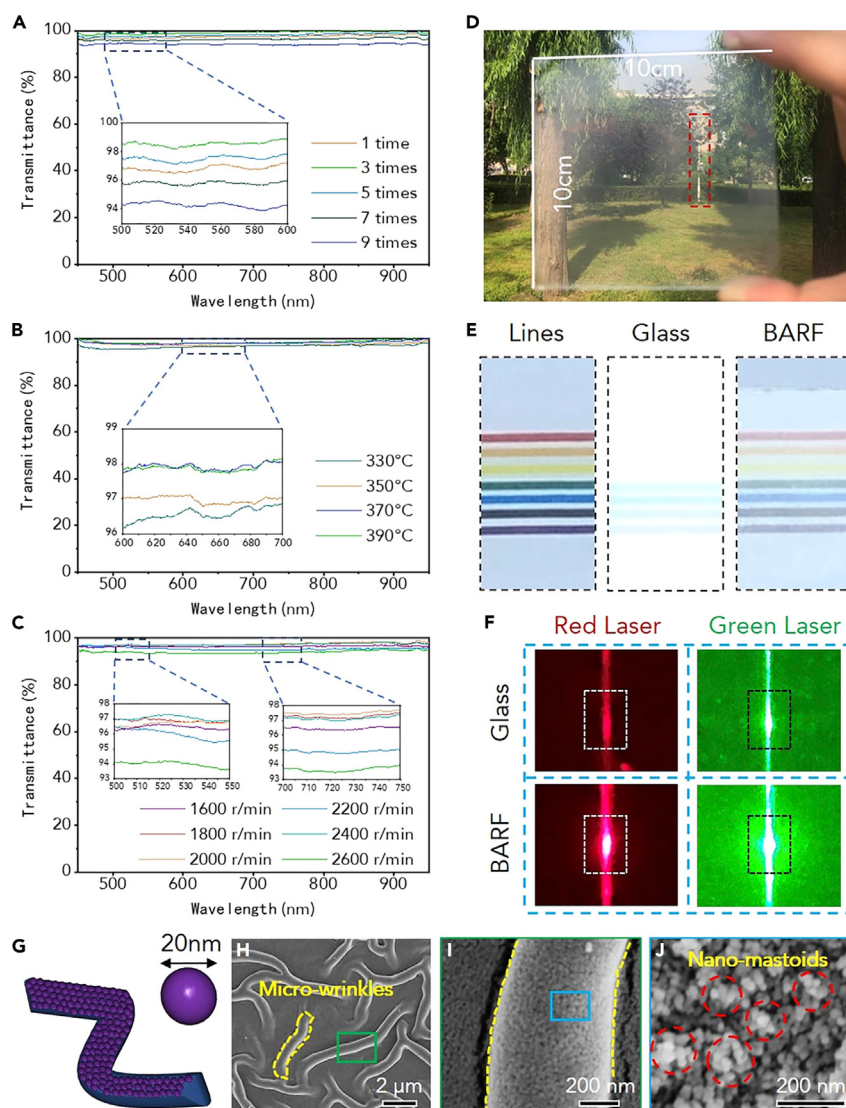


**Figure 3. Basic antireflective performance of BARFs**

(A) Transmittance spectra of the BARFs prepared at different spin-coating times. The inset demonstrates that the transmittance reached the maximum when the spin-coating process was carried out three times.

(B) Transmittance spectra of the BARFs prepared at a gradient temperature from 330°C to 390°C with intervals of 20°C. The inset illustrates that the optimal annealing temperature was 370°C.

(C) Transmittance spectra of the BARFs prepared at a gradient spin-coating speed from 1,600 to 2,600 r/min with intervals of 200 r/min. The inset shows that the optimal spin-coating speed was 2000 r/min.

(D) A large-scale glass slide coated with BARF (10 × 10 cm). The red dashed box highlights that a telegraph pole can be clearly observed through the BARF-coated glass slide under strong light condition.

(E) Anti-glare behavior of BARF.

(F) Digital images of glass slides and BARF illuminated with red and green laser beams.

(G) Structural models of microscale wrinkle and nanoscale sphere. The wrinkle is made up of nanospheres.

(H–J) SEM images of hierarchical structures distributed on the BARF surface.

Figures 3A–3C show the transmittance of BARF with different variables (spin-coating times, annealing temperature, spin-coating speed). Figure 3A shows the transmittance of BARF under different times of spin-coating. It can be seen from the five transmittance curves that the transmittance first increased and then decreased

with the increase in spin-coating time. The increase in spin-coating time could lead to an increase in BARF thickness. More importantly, the thickness of BARF with a micro-nano structure is very critical for its AR ability. For better optical performance, the film thickness should be fabricated to the appropriate size that coordinates the RI of the material used in the process. By observing the position of the five curves in the figure, we see that the BARF possesses the highest transmittance when spin-coated three times. Therefore, three bouts of spin-coating was chosen as the optimum process to fabricate the BARF.

As for annealing temperature, [Figure 3B](#) shows the transmittance of BARF fabricated under different annealing temperatures at a spin-coating speed of 2,000 r/min. The annealing temperature affects the microscale wrinkle density on the BARF surface. And the density changes in the microscale wrinkles leads to different optical properties. It can be seen that with the increase in annealing temperature, the transmittance of BARF increases gradually. When the temperature reached 370°C, the transmittance reached the highest, about 97%. It is interesting that, when the temperature rose to 390°C, the transmittance curve did not show an obvious increasing trend and even almost coincided with the curve at 370°C. Combined with the density of wrinkles at different temperatures ([Figures 2B–2D](#)), it could be concluded that the density of the wrinkles plays an important role in optical performance. In addition, nanospheres on the BARF surface were not distinct or clear enough at low temperature. But as the temperature increased, the boundaries of the nanospheres became clearer ([Figure S3](#)). Based on the above results and conditions, the BARF obtained the highest transmittance under an annealing temperature of 370°C during the fabrication process and possessed a distinct structural integrity of the nanospheres. As mentioned above, the spin-coating speed influenced the thickness of the BARF, which affected optical performance. As can be seen from [Figure 3C](#), with the increase in spin-coating speed, transmittance first increased and then decreased. When the spin-coating speed reached 2,000 r/min, the transmittance of the BARF was the highest ([Figure S4](#) shows the transmittance of the BARF at 330°C, 350°C, and 390°C with different spin-coating speeds). Referring to the surface topography in [Figure S1](#), 2,000 r/min was selected to fabricate BARF on the glass substrate.

[Figures 3D–3F](#) show the optical properties of the glass slide with BARF as well as visual pictures. [Figure 3D](#) exhibits a glass slide with a hierarchically architected bioinspired ZnO thin film fabricated on its surface under optimal fabrication conditions. The optimal fabrication conditions were as follows: spin-coating three times, spin-coating speed 2,000 r/min, and maintenance at 370°C for 30 min. The dimensions of the glass slide with BARF are shown in [Figure 3D](#), which was taken with a cell phone. As can be seen from the figure, this kind of antireflective glass slide had excellent visual imaging ability. The scenery on the other side of the glass could be displayed through the slide. What is more, the communications facility about 10 m away from the shooting site was still clearly visible.

Anti-glare ability was one of the important indicators for the BARF. BARFs with superior anti-glare ability could be used in strong light conditions to increase clarity to achieve a better visual effect. [Figure 3E](#) shows the consequences of the glass slide with BARF compared with normal glass under strong light. When there was no glare, both the glass slide and the BARF-coated glass slide could present the color lines below. However, under conditions with strong light, it was difficult to see the lines below through a normal glass slide surface, but the BARF worked so well that the lines below could still be seen. When the colored curves were replaced by various color words underneath the glass slide and glass slide coated with BARF,

the anti-glare ability was still highlighted through the images, as shown in [Figure S5](#). Eight colors were selected to test the visual conditions. As can be seen from the eight images, when it came to light colors, the vision was partially lost. However, the vision was better when the text was dark. The red and green lasers were then used to test the light intensity of light penetrating through a BARF. The results are shown in [Figure 3F](#). From the two sets of images, it can be revealed that a laser propagating through the BARF increased multiangle reflection of the surface, thus reducing the intensity of the directly reflected light.

The model of the microscale-wrinkle structure with nanospheres is shown in [Figure 3G](#). The nanospheres were about 20 nm in diameter, and they were found clearly on wrinkles and other smooth areas. [Figures 3H–3J](#) show the surface structure of the BARF at different magnifications. It can be seen from the images that the BARF surface is wholly covered with microscale wrinkles assembled of homogeneous ZnO nanospheres. The wrinkles are randomly architected, and one wrinkle connects to another or more. Most of the wrinkles are about 10  $\mu\text{m}$  in length, with a few less than 4  $\mu\text{m}$ . It can also be found that the area between the wrinkles presents a smooth plane, which has different shapes due to the random distribution of wrinkles. Moreover, [Figure S6](#) shows that the thickness of the BARF is between about 280 and 500 nm.

#### FDTD simulation of optical properties of BARF

To verify the effectiveness of biomimetic feature structures, finite-difference time-domain (FDTD) simulation was carried out. [Figures S7](#) and [S8](#) illustrate the structural models and simulation results of three kinds of structures in terms of transmittance. The three structures were plane structure (PS; [Figure S7A](#)), wrinkle structure (WS; [Figure S7B](#)), and WS formed by the stack of nanoparticles (WS-NPs; [Figure S7C](#)). The structural parameters of WS and WS-NPs were obtained from the SEM images of BARF. In particular, the diameter of the nanoparticles was 20 nm in WS-NPs, which was consistent with the measured data in [Figure 3G](#). The simulation results of transmittance are presented in [Figures S7D–S7F](#). It can be seen that the WS effectively enhanced the light transmittance in the short wavelength and reduced the reflectance in the same region. When it came to the WS-NPs, the transmittance showed a stronger enhancement in the broad band compared with PS and WS. Considering the simulation processes in [Figures S8A–S8I](#), the concave region in the WS could effectively lead to an energy concentration effect. What is more, the nanoparticles in WS-NPs could further increase the transmittance of light, thereby achieving the optimum AR efficiency.

#### Omnidirectional antireflective property of BARF

Among the feature functions of antireflective films, omnidirectional AR is more favorable for practical applications, as the sunlight angle is changing all the time. As shown in [Figure 4](#), the angular dependence of the glass slide with BARF was examined through a spectrometer. The glass slide was placed neatly between the incident light and the light detector, and the side with BARF faced the incident light. When the incident light was perpendicular to the BARF ([Figure 4A](#)),  $\beta$  was 0°, and  $\alpha$  gradually increases to 360°, the glass slide was rotated along the x axis to measure its transmittance at this point. As we can see from the curves, there was little difference in transmittance from different angles. Then the glass was tilted slowly along the y axis ([Figure 4B](#)),  $\alpha$  kept at 0°, and  $\beta$  gradually increased. Remarkably, as  $\beta$  increased to 45°, it can be seen from the figure that the transmittance hardly decreased. When  $\beta$  increased to 75°, the transmittance of the glass slide decreased by less than 5%. Next,  $\beta$  was kept at 45° and  $\alpha$  gradually increased to 360° ([Figure 4C](#)). The transmittance curves hardly showed any difference.

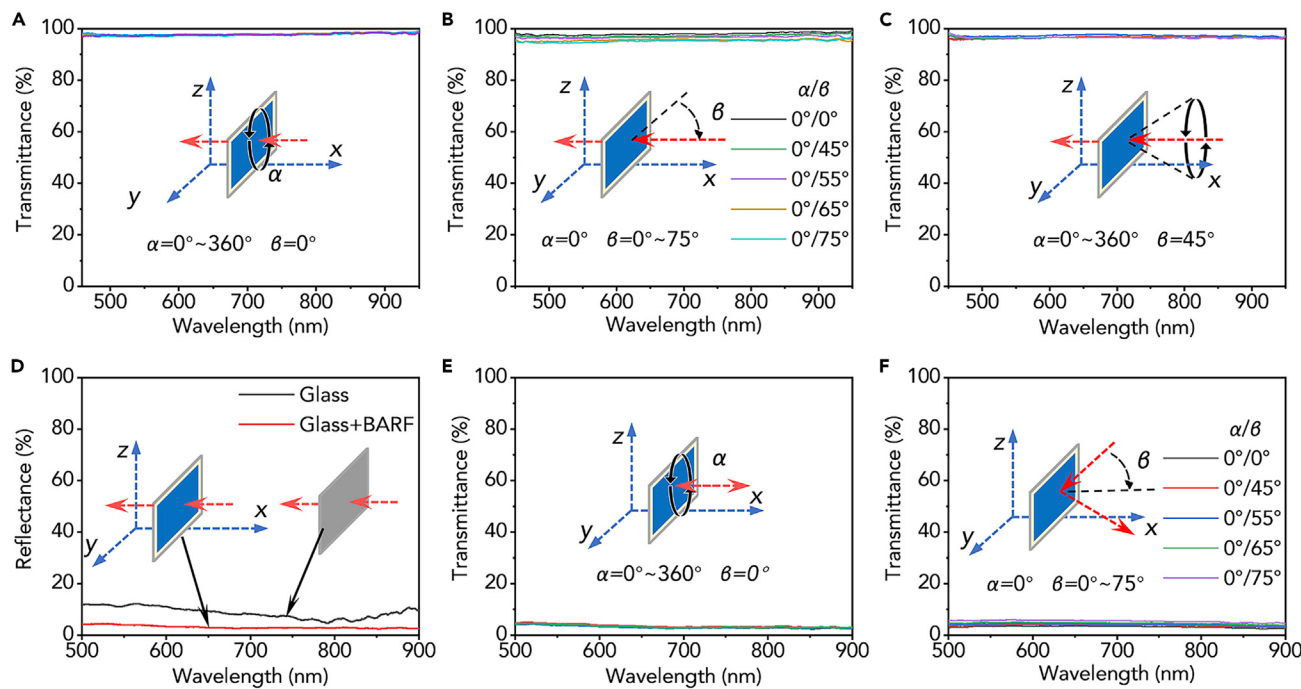


**Figure 4. Omnidirectional antireflective performance of BARF**

(A–C) Angle-resolved spectrometry characterizing the angular transmittance properties of BARF.

(D) Reflectance spectrum of glass slides with and without BARF.

(E and F) Angle-resolved spectrometry characterizing the angular reflectivity properties of BARF.

Similarly, the reflectance of the glass slide was tested under the same conditions. It is worth noting that the reflectance of a glass slide with BARF is only about 4%, while that of normal glass is 10% (Figure 4D;  $\beta$  is  $0^\circ$  and  $\alpha$  is  $0^\circ$ ). When the reflectance was tested, the test position was located at the same position as the light source, and the reflection data of the glass slide were obtained. Figure 4E shows almost no difference in the reflectance at different angles ( $\alpha$  increased from  $0^\circ$  to  $360^\circ$ ) when the light is perpendicular to the glass slide surface ( $\beta$  is  $0^\circ$ ). Figure 4F shows that when the incident angle of the light source gradually increases (the glass slide is rotated along the  $y$  axis,  $\alpha$  is  $0^\circ$  and  $\beta$  increases from  $0^\circ$  to  $75^\circ$ ), the reflected light is really weak, so that the reflection curve is barely visible in the figure. This unique omnidirectional antireflective property, which originates from the randomly distributed microscale WSs on the surface and close-packed nanospheres, suggests that the hierarchically architected structure could reduce AR under large-angle irradiation.

#### Photoelectric conversion performance of a solar panel coated with BARF

Organic solar cells and perovskite cells are getting more and more attention for their record-breaking photoelectric conversion efficiency. Many researchers have delved into the light absorption layer and electron transport layer inside the solar cells, so as to improve the power conversion efficiency (PCE). For instance, Lan et al. have successfully fabricated a variety of modules to improve the PCE of organic solar cells.<sup>51–53</sup> However, organic solar cells and perovskite cells have some limitations in large-scale practical applications. Hence, we prepared BARF on the surface of a polycrystalline silicon solar panel ( $5.2 \times 5.2$  cm), which is the type widely used now.

Usually, traditional solar panels are covered with a conformal coating. Its function is to protect circuit boards and related equipment from environmental damage.

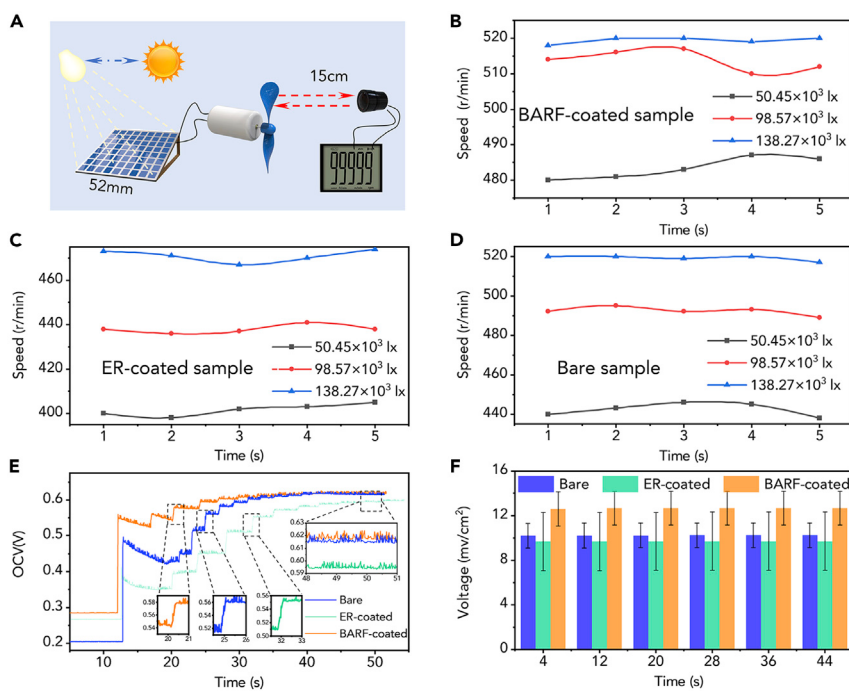


**Figure 5. Photoelectric conversion performance of the solar panel coated with BARF**

- (A) Schematic illustration of the self-built system for investigating the light-trapping efficiency.
- (B) Rotation speed of a mini-fan driven by a solar panel coated with BARF under different lighting conditions.
- (C) Rotation speed of a mini-fan driven by a solar panel coated with the epoxy film under different lighting conditions.
- (D) Rotation speed of a mini-fan driven by a bare solar panel under different lighting conditions.
- (E) OCV of three solar panels under different lighting conditions.
- (F) Average voltage per unit area generated by three solar panels.

Acrylic resin or silicone resin is the main component of conformal coating. According to the different components, trial curing, thermal curing, and UV curing are the main methods to achieve the encapsulation process. In the experiment, commercial epoxy resin (ER) was chosen to fabricate a conformal coating directly on solar panels by heat curing. Coupled with solar panels covered with no film, the three kinds of solar panels were then tested and compared.

Figure 5A shows a schematic diagram of the test setup. Instead of sunlight, three kinds of solar panels were illuminated to provide power for the rotation of the mini-fan. An infrared velocimeter took measurements at 15 cm directly opposite the mini-fan. During the test, the light intensity was changed to test the fan speed under different output voltages. Light intensity was classified according to energy level as weak light ( $50.45 \times 10^3$  lx), medium light ( $98.57 \times 10^3$  lx), and strong light ( $138.27 \times 10^3$  lx). Light intensities are shown in Figure S9A. Figures 5B–5D show the rotation speed of the mini-fan powered by a BARF-coated solar panel, a bare solar panel, and an ER-coated solar panel under three light intensities. The mini-fan showed the fastest rotation speed at all three kinds of light intensity when powered by a BARF-coated solar panel, showing an excellent power supply effect (Figure S10). Under strong light condition, the rotation speed of the mini-fan powered by a bare solar panel is close to the rotation speed of the mini-fan powered by a BARF-coated solar panel. Compared with the mini-fan powered by an ER-coated solar panel, the rotation speed of the mini-fan powered by a BARF-coated solar panel is increased by

about 20% under the weak light conditions, 17% under medium light conditions, and 10% under strong light conditions.

**Figure 5E** shows the open-circuit voltage (OCV) of three kinds of solar panels under varying light intensity. The light brightness was gradually increased by buttons. There are six clear phase steps in each curve. The intensity of light continued to increase, but it was difficult to see a noticeable change in the three curves. At the initial state, the solar panel with BARF had the highest OCV. Due to the instability of the light source, there was a weakening of the light immediately after it was turned on, which caused a brief dip in the three curves. When the light intensity was at its highest, the solar panel with BARF still generated the highest OCV, about 0.62 V. An ER film coating on the surface can enhance the mechanical durability of solar panels. However, a considerable amount of incident light is reflected by the flat ER surface. In addition, the ER film can lead to a sudden change in RI, which also affects the OCV of ER-coated solar panels. Therefore, the OCV for the ER-coated solar panels was much lower than for the bare ones.

Then, the voltage per unit area generated by the three solar panels under indoor lighting was compared, which is shown in **Figure 5F** (the detailed voltages generated by the three kinds of panels are shown in **Figures S9B–S9D**). The BARF-coated solar panel demonstrates superior enhancement of performance. Compared with the ER-coated solar panel, the voltage generated by the BARF-coated solar panels per unit area is higher by 30.48%. When it comes to bare solar panels, the enhancement effect reaches 23.85%. And the voltage of the BARF-coated solar panel is very stable. The voltage in **Figure 5E** has no obvious fluctuation phenomenon as time goes on. In addition, the current density of the solar panels coated with BARF also shows an increasing trend, as shown in **Figure S11**. **Figures S11A–S11C** show the current density results under a 138.27 lx light intensity. And **Figures S11D–S11F** show the current density results under a 50.45 lx light intensity. Under both light intensities, the BARF improved the current density of the solar panels.

**Figure 6** demonstrates the performance of three kinds of solar panels under standard lighting conditions (in the lab, air-mass (AM) 1.5) and outdoor sunlight. Under the standard light conditions, the J-V characteristic curve of solar panels can be obtained by changing the external resistance. As shown in **Figure 6A**, the OCV and short-circuit current ( $I_{sc}$ ) of the BARF-coated solar panel are increased obviously compared with the bare sample and ER-coated sample. The peak OCV and  $I_{sc}$  are 648.8 mV and 353.85 mA, respectively. The bare solar panel possesses the middle OCV and  $I_{sc}$ , which are 597.82 mV and 316.77 mA, respectively. As for the ER-coated solar panel, it shows the lowest performance (565.93 mV and 283.82 mA). The solar panel coated with BARF has a PCE of 2.14%. As for the bare solar panel, it features a middle PCE of 1.76%. When the solar panel is coated with ER film, it shows the lowest PCE of 1.50%. **Figure 6B** shows the output power curves of the three solar panels. The BARF-coated solar panel also features the highest output power, which is about 57.74 mW. It is followed by the bare solar panel, which is about 47.62 mW. As for the ER-coated solar panel, its output power is about 40.64 mW. The fill factors (FFs) of the three kinds of solar panels are also calculated. When the output power of the solar cell reaches the maximum, the ratio of the product of current and voltage to the product of  $I_{sc}$  and OCV is defined as the fill factor. According to the J-V characteristic curves in **Figure 6A**, it can be obtained that the fill factors of all three kinds of solar panels are about 25. This could indicate that the BARF does not change the essential properties of the solar panels. The BARF only reduces the reflection and enhances the transmittance of light on the surface, yet significantly improves the OCV,  $I_{sc}$ , and output power of solar panels. **Figures 6C–6E** show the three solar panels with different films and their

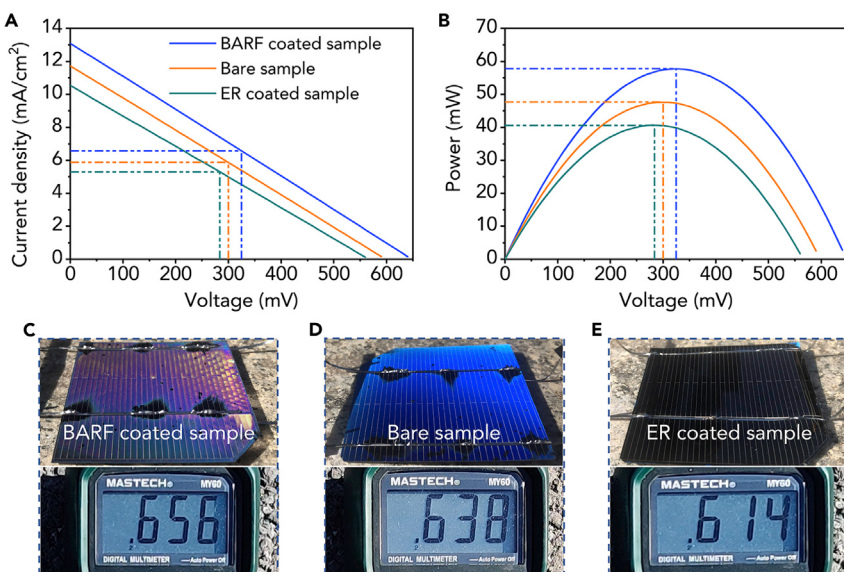


**Figure 6. Performance of solar panels under standard illumination (AM 1.5) and outdoor light conditions**

(A) J-V characteristic curves of three kinds of solar panels in the standard test environment.  
(B) The output power curves of three kinds of solar panels in the standard test environment.  
(C-E) Digital images of the three solar panels and corresponding OCV tested under natural sunlight.

corresponding OCV. Under the same outdoor lighting conditions, the BARF-coated solar panel has the highest OCV, generating 656 mV. However, ER-coated solar panels produced the lowest voltage, 614 mV. In conclusion, this BARF could increase the output voltage of solar panels and provide stronger photoelectric conversion capability, thus realizing efficient light energy utilization.

To increase the light energy absorption and PCE of polycrystalline silicon solar panels, some efficient AR films have already been developed.<sup>54–56</sup> The enhancement of the PCE of these AR films reaches about 0.1%. As for the BARF, the PCE of solar panels coated with it could be improved by 0.38% (from 1.76% to 2.14%). Moreover, the BARF possesses better mechanical durability than those in previous publications.

### Scratching tests of BARF

Figure 7 shows the wear resistance of this kind of BARF. Considering the practical applications of antireflective films, they are often damaged by physical factors such as friction or scratches. When physical damage occurs, whether the optical performance and film integrity could maintain the same properties as before is an important reference for the quality of BARFs. The mechanical stability of a BARF was assessed by a scratching test. The relevant dimensions of the scratching machine are shown in Figure 7B. The scratching test included the following three steps. First, the scratching machine was taken to line out scratches on the BARF to break the surface integrity (Figure 7A). Then, we pasted the film with tape over the scratches five times. Next, the surface morphology of the BARF was observed, and the optical property was tested through a spectrograph. As we can see from the illustration in Figure 7F, the ultra-depth-field microscope image shows that the scratches are very clear and there is no film falling off after the scratching test. Figures 7C and 7D show the surface 3D depth before and after the scratching test (Figure S12 shows the SEM images before and after the scratching test). Some areas have no residual film after scratching, which is shown in blue. The rest of the slide is evenly covered

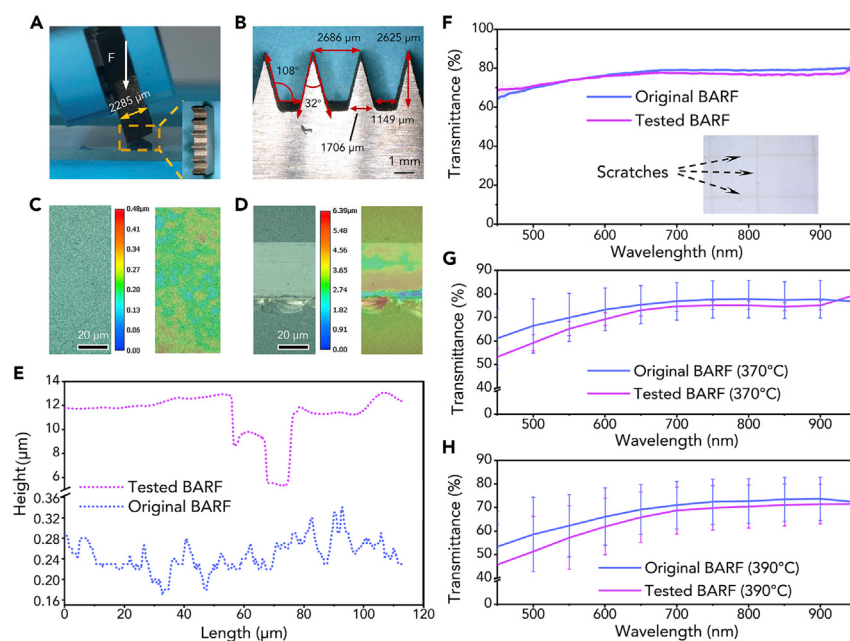


**Figure 7. Mechanical durability of BARF investigated through scratching tests**

- (A) Schematic illustration of the scratching test.
- (B) Dimensions of the scratcher blade.
- (C and D) Surface topographies of the BARF before and after the scratching test.
- (E) Surface profile perpendicular to the scratching direction.
- (F) Transmittance of a glass slide with BARF before and after scratching test. The inset image shows a scratched glass slide with BARF.
- (G and H) Transmittance of a scratched glass slide with BARF under different annealing temperatures. Error bars show SD between replicates ( $n = 5$  masks for each type tested).

with ZnO film. Figure 7E is the surface topography curve for BARF before and after the scratching test. The depth of the scratch is about 6  $\mu\text{m}$  and its width is about 20  $\mu\text{m}$ . Moreover, the maximum surface height difference is 0.32  $\mu\text{m}$ , except for scratch. The height of this microscopic surface structure also indicates that the surface of the hierarchical structure is almost flat at the nanometer scale.

Figure 7F shows the transmittance of the glass slide (~1 mm) with a BARF before (original BARF) and after (scratched BARF) the scratching test. At the short wavelength, the scratched BARF is slightly higher than the original BARF. Then the curves are nearly overlapping in the rest of the region. Their maximum difference is only about 2% between 800 and 900 nm. Figures 7G and 7H show the comparison of data at particular points. After the scratching test, the BARF did not shed a large number of layers, but there was still a very tiny amount of ZnO attached, which resulted in the curve after the scratching test being slightly lower than the original one. Figures S12A and S12B are the SEM images before the operation, and Figures S12C and S12D are the images after the operation. From the comparison images at different magnifications, it could be seen that after the operation, the WSs on the surface did not deform or fall off. The ZnO nanospheres on the wrinkle and flat area are still clearly visible, which is enough to show the excellent wear resistance of the BARF.

#### Falling-sand tests of BARF

In the face of natural falling-sand conditions, the resistance of BARF is also very critical. The transmittance of the glass slide with BARF under the conditions of falling sand was tested accordingly. Anti-reflection film was fabricated on square glass

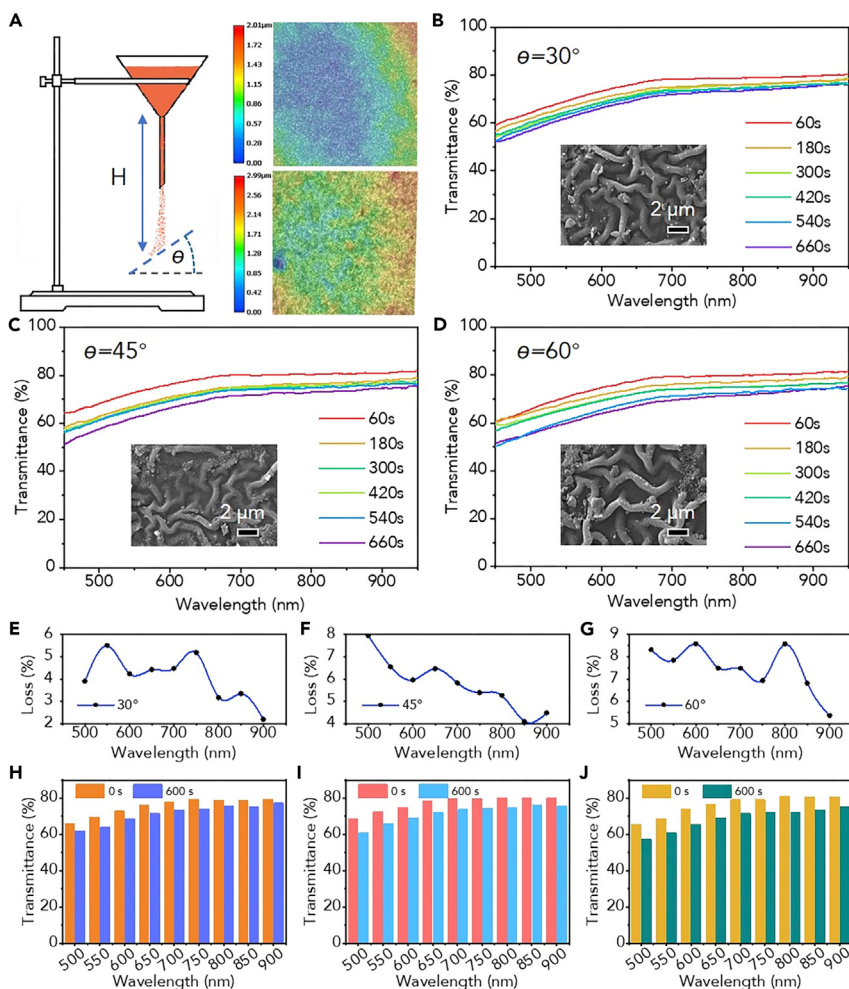


**Figure 8. Mechanical durability of BARF investigated through falling-sand tests**

(A) Schematic diagram of the falling-sand test. The images on the right show the surface topographies of BARFs before and after the falling-sand test.

(B–D) Transmittance of glass slides with BARF under different inclination angles.

(E–G) Transmittance loss of glass slides with BARF under different inclination angles.

(H–J) Statistical charts of the transmittance of glass slides with BARF before and after the falling-sand tests under different inclination angles (30°, 45°, and 60°, respectively).

sheets with a side length of 4 cm through the method mentioned above. Then the glass slides were tilted at different angles (30°, 45°, 60°) on the special platform. The sand fell freely by gravity at a height of 65 cm from the funnel, striking the BARFs. Figure 8A shows the schematic diagram of the falling-sand process. The two 3D insets show the surface topography of the BARF before and after sand falling at 30° (Figure S13 shows the surface topography of BARFs at 45° and 60°). Figure S14 shows the SEM image of the original BARF. The insets of Figures 8B–8D show the surface morphology after falling-sand tests. It can be seen from the morphology that with the increase in falling-sand angle, the regional integrity is gradually affected. When the falling-sand angle is 30°, the BARF can still maintain a relatively complete morphology. However, the morphology is slightly damaged in the other two angles.

Figures 8B–8D show the transmittance of the glass slide with BARF at different wavelengths under different tilted angles (30°, 45°, 60°). From short to long wavelengths,

the transmittance of the glass slide with BARF increases gradually, and the fluctuation range of transmittance decreases with the increase in wavelength. At 450 nm, the transmittance fluctuates greatly with the increase in sand falling time. As for long wavelengths, the fluctuation of transmittance decreases significantly, and transmittance attenuation is only about 2%, which is shown in Figures 8E–8G. The influence of falling sand is more obvious at short wavelengths, but the whole curve shows a certain attenuation according to the test wavelength range. More important, as the angle of falling sand increases, that is, the tilted angle increases, the decline in transmittance increases gradually. When the tilted angle is 30°, from 500 to 900 nm, the decline rate decreases from 6% to about 2%. When it comes to 60°, the decline rate decreases from 8% to about 5%. In practical applications, the angle between the sand and the BARF should be kept as small as possible to reduce the reduction in transmittance. Figures 8H–8J show the transmittance of glass slides under different wavelengths at the beginning and end of the sand falling. It can be concluded that, with the increase in wavelength, the transmittance of the glass slides with BARF before and after the falling-sand test tends to increase.

### Conclusion

In summary, an ommateum-inspired hierarchically architected ZnO film integrating omnidirectional AR and mechanical durability was successfully prepared through a method combining layer-by-layer thermal decomposition and *in situ* self-assembly. Employing multiscale morphology observations, it was demonstrated that ZnO particles were stacked compactly, building up nanoscale sphere arrays and microscale irregularly distributed wrinkles for the BARF. With the help of various optical characterizations, it was confirmed that the BARF exhibited a transmittance over 95% in light incident angles from –75° to 75°. This excellent BARF endowed the solar cells with a superior antireflective capacity and photoelectric conversion rate, which was 30.48% higher than those coated by commercial AR films. Furthermore, the mechanical durability of the BARF was illustrated through scratching and falling-sand tests. The compact arrangement of ZnO nanospheres and strong interface binding force prevented the exquisite architecture from shedding and being destroyed. Remarkably, the BARF demonstrated excellent mechanical durability in the full spectrum (~2% transmittance loss). The combined advantages of superior AR, scalable manufacturing, excellent durability, and non-toxicity make our integrated design promising for fabricating large-scale omnidirectional AR films that are suitable for practical photovoltaic power generation and anti-glare of sophisticated optical instruments.

## EXPERIMENTAL PROCEDURES

### Resource availability

#### Lead contact

The lead contact for this article is Shichao Niu, [niushichao@jlu.edu.cn](mailto:niushichao@jlu.edu.cn).

#### Materials availability

This study did not generate new unique materials.

#### Data and code availability

The data presented in this work are available from the [lead contact](#) upon reasonable request.

### Materials

The red dragonfly was purchased from Taobao. Sodium hydroxide was provided by Beijing Chemical Works. 2-Methoxyethanol (CAS: 109-86-4) and ethanolamine (ETA,

CAS: 141-43-5) were purchased from Aladdin. Ethanol absolute was provided by Tianjin Jingdongtianzheng Precision Chemical Reagent Factory. Mini-motor, mini-fan, and untreated solar panels were purchased from Taobao. An infrared velocimeter (TA8146C) was bought from Taobao. In this work, the thickness of the glass used for the scratching test and the falling-sand test was 1 mm, and the thickness of the rest of the glass slide was 0.17 mm. For strength consideration, the glass slide thickness of Figure 3D was also selected as 1 mm. As for the cleaning process, first of all, the normal slide was cut into a square block with sides of 2.5 cm. Then, the glass slices were successively washed with sodium hydroxide solution, deionized water, and anhydrous ethanol ultrasonically for 5 min. The mass fraction of the sodium hydroxide solution was 2%. Finally, the cleaned glass slides were placed horizontally in a clean petri dish and dried at 80°C for the next step.

### Solution preparation

The viscosity of the ZnO aqueous solution was very small, and it was difficult to adhere to the glass surface. Therefore, ethylene glycol methyl ether (2-methoxyethanol) was selected as the solvent to prepare the ZnO acetate solution. ETA was selected as the solution stabilizer to help the ZnO acetate disperse more evenly. 2-Methoxyethanol (100 mL) was poured into a beaker. Then, 21.94 g of  $Zn(CH_3COOH)_2 \cdot 2H_2O$  was weighed with a balance into the solvent. Next, 6.10 g of ETA was extracted with a straw and dropped into the mixed solution. Finally, the magnetic stirring was done for 30 min at 60°C. The solution then stood still in the backlight for 6 h waiting for the next operation.

### Spin-coating and preliminary heating

The cleaned glass slide was taken out, and 0.5 mL of the aging mixed solution at a time was added onto the slide with a straw. Then, the spin-coating speed was set differently for the coating treatment. In the experiment, the speed ranged from 1,600 to 2,600 r/min, at intervals of 200 r/min. Next, the slides were heated at 80°C for 10 min. The operation was repeated another two times.

### Annealing treatment

Annealing treatment needed to be carried out in a muffle furnace. It is difficult for ordinary ovens to achieve temperatures close to 400°C. Immediately after the above operation, the glass slides were put into the muffle furnace. Then, the temperature was raised by 5° per minute. After the maximum temperature was reached, the temperature was maintained for 30 min and then cooled down with the furnace naturally. The maximum temperature of the annealing process ranged from 330°C to 390°C, increasing by 20°C.

### Characteristics of the feature structures of dragonfly ommateum and BARF

With the help of an ultra-depth microscope (VHX-S650E), the morphologies and dimensions of the BARF were characterized under different magnifications. The dragonfly eyes and BARFs were visualized by SEM (JSM-6700F, JEOL). In addition, the detailed structure parameters of wrinkles and nanomastoid were obtained under increasing magnification.

### Reflectance and transmittance spectra

The reflectance spectra of the dragonfly eyes and transmittance spectra of the BARF were obtained using a miniature fiber-optic spectrometer (Ocean Optics USB4000), and the light spot size of the incident beam was about 5 mm in diameter. The spectrometer was carefully calibrated using STD-WS, a standard whiteboard certified by the National Institute of Metrology of China.

## SUPPLEMENTAL INFORMATION

Supplemental information can be found online at <https://doi.org/10.1016/j.matt.2022.06.015>.

## ACKNOWLEDGMENTS

The Foundation for Innovative Research Groups of the National Natural Science Foundation of China (52021003), the National Natural Science Foundation of China (51875244, U19A20103, 52105301), the Jilin University Science and Technology Innovative Research Team (2020TD-03), and "Fundamental Research Funds for the Central Universities" supported this work.

## AUTHOR CONTRIBUTIONS

Z.H., S.N., B.L., and H.D. conceived the idea and designed the experiments. H.D. and Z.W. performed the experiments and characterization. S.N., B.L., H.D., and Z.W. helped with data analysis and theoretical simulation. L.R. and Z.H. proposed the mechanism of the bioinspired materials. B.L. and H.D. wrote the paper.

## DECLARATION OF INTERESTS

The authors declare no competing interests.

Received: February 14, 2022

Revised: May 16, 2022

Accepted: June 7, 2022

Published: June 28, 2022

## REFERENCES

1. Hao, Z., Jiang, T., Lu, Y., Feng, S., Shen, R., Yao, T., Yan, Y., Yang, Y.M., Lu, Y., and Lin, S. (2019). Co-harvesting light and mechanical energy based on dynamic metal/perovskite Schottky junction. *Matter* 1, 639–649. <https://doi.org/10.1016/j.matt.2019.05.003>.
2. Kim, M., Yi, S., Kim, J.D., Yin, X., Li, J., Bong, J., Liu, D., Liu, S.C., Kvit, A., Zhou, W., et al. (2018). Enhanced performance of Ge photodiodes via monolithic antireflection texturing and  $\alpha$ -Ge self-passivation by inverse metal-assisted chemical etching. *ACS Nano* 12, 6748–6755. <https://doi.org/10.1021/acsnano.8b01848>.
3. Tavakoli, M.M., Tsui, K.H., Zhang, Q.P., He, J., Yao, Y., Li, D.D., and Fan, Z.Y. (2015). Highly efficient flexible perovskite solar cells with antireflection and self-cleaning nanostructures. *ACS Nano* 9, 10287–10295. <https://doi.org/10.1021/acsnano.5b04284>.
4. Jiang, H., Tong, L., Liu, H., Xu, J., Jin, S., Wang, C., Hu, X., Ye, L., Deng, H., and Cheng, G.J. (2020). Graphene-metal-metastructure monolith via laser shock-induced thermochemical stitching of MOF crystals. *Matter* 2, 1535–1549. <https://doi.org/10.1016/j.matt.2020.03.003>.
5. Wu, S., Xiong, G., Yang, H., Tian, Y., Gong, B., Wan, H., Wang, Y., Fisher, T.S., Yan, J., Cen, K., et al. (2019). Scalable production of integrated graphene nanoarchitectures for ultrafast solar-thermal conversion and vapor generation. *Matter* 1, 1017–1032. <https://doi.org/10.1016/j.matt.2019.06.010>.
6. Xiao, C., Zhang, F., Li, Z., Harvey, S.P., Chen, X., Wang, K., Jiang, C.S., Zhu, K., and Al-Jassim, M. (2020). Inhomogeneous doping of perovskite materials by dopants from hole-transport layer. *Matter* 2, 261–272. <https://doi.org/10.1016/j.matt.2019.10.005>.
7. Zhang, D., Wang, J., Tong, Z., Ji, H., and Qu, H.Y. (2021). Bioinspired dynamically switchable PANI/PS-b-P2VP thin films for multicolored electrochromic displays with long-term durability. *Adv. Funct. Mater.* 31, 2106577. <https://doi.org/10.1002/adfm.202016577>.
8. Eiamchai, P., Horprathum, M., Patthanasettakul, V., Limnonthakul, P., Nuntawong, N., Limsuwan, P., and Chindaodom, P. (2010). Designs and investigations of anti-glare blue-tint side-view car mirrors. *Mater. Design* 31, 3151–3158. <https://doi.org/10.1016/j.matdes.2010.02.033>.
9. Liu, B.T., and Teng, Y.T. (2010). A novel method to control inner and outer haze of an anti-glare film by surface modification of light-scattering particles. *J. Colloid Interf. Sci.* 350, 421–426. <https://doi.org/10.1016/j.jcis.2010.07.014>.
10. Liu, L.Q., Wang, X.L., Jing, M., Zhang, S.G., Zhang, G.Y., Dou, S.X., and Wang, G. (2012). Broadband and omnidirectional, nearly zero reflective photovoltaic glass. *Adv. Mater.* 24, 6318–6322. <https://doi.org/10.1002/adma.201201740>.
11. Papadopoulos, A., Skoulas, E., Mimidis, A., Perrakis, G., Kenanakis, G., Tsibidis, G.D., and Stratakis, E. (2019). Biomimetic omnidirectional antireflective glass via direct ultrafast laser nanostructuring. *Adv. Mater.* 31, 1901123. <https://doi.org/10.1002/adma.201901123>.
12. Balazadeh Koucheh, A., Kecebas, M.A., and Sendur, K. (2021). Impedance mismatch-based enhancement of broadband reflectance of tungsten with bio-inspired multilayers. *J. Quant. Spectrosc. Radiat. Transf.* 276, 107899. <https://doi.org/10.1016/j.jqsrt.2021.107899>.
13. Shi, J., Zhang, J., Yang, L., Qu, M., Qi, D.C., and Zhang, K.H.L. (2021). Wide bandgap oxide semiconductors: from materials physics to optoelectronic devices. *Adv. Mater.* 33, 2006230. <https://doi.org/10.1002/adma.202006230>.
14. Shih, M.S., Chen, H.Y., Li, P.C., and Yang, H. (2020). Broadband omnidirectional antireflection coatings inspired by embroidered ball-like structures on leafhoppers. *Appl. Surf. Sci.* 532, 147397. <https://doi.org/10.1016/j.apsusc.2020.147397>.
15. Dong, X., Si, Y., Chen, C., Ding, B., and Deng, H. (2021). Reed leaves inspired silica nanofibrous aerogels with parallel-arranged vessels for salt-resistant solar desalination. *ACS Nano* 15, 12256–12266. <https://doi.org/10.1021/acsnano.1c04035>.
16. Han, Z.W., Wang, Z., Li, B., Feng, X.M., Jiao, Z.B., Zhang, J.Q., Zhao, J., Niu, S.C., and Ren, L.Q. (2019). Flexible self-cleaning broadband antireflective film inspired by the transparent cicada wings. *ACS Appl. Mater. Interfaces* 11, 17019–17027. <https://doi.org/10.1021/acsm.9b01948>.

17. He, Z., Wu, C., Hua, M., Wu, S., Wu, D., Zhu, X., Wang, J., and He, X. (2020). Bioinspired multifunctional anti-icing hydrogel. *Matter*, 2, 723–734. <https://doi.org/10.1016/j.matt.2019.12.017>.
18. Huang, Z., Cai, C., Kuai, L., Li, T., Huttula, M., and Cao, W. (2018). Leaf-structure patterning for antireflective and self-cleaning surfaces on Si-based solar cells. *Sol. Energy* 159, 733–741. <https://doi.org/10.1016/j.solener.2017.11.020>.
19. Isakov, K., Kauppinen, C., Franssila, S., and Lipsanen, H. (2020). Superhydrophobic antireflection coating on glass using grass-like alumina and fluoropolymer. *ACS Appl. Mater. Interfaces* 12, 49957–49962. <https://doi.org/10.1021/acsami.0c12465>.
20. Han, Z.W., Mu, Z.Z., Li, B., Wang, Z., Zhang, J.Q., Niu, S.C., and Ren, L.Q. (2016). Active antifogging property of monolayer  $\text{SiO}_2$  film with bioinspired multiscale hierarchical pagoda structures. *ACS Nano* 10, 8591–8602. <https://doi.org/10.1021/acsnano.6b03884>.
21. Yin, K., Song, Y.X., Dong, X.R., Wang, C., and Duan, J.A. (2016). Underwater superoleophobicity, anti-oil and ultra-broadband enhanced absorption of metallic surfaces produced by a femtosecond laser inspired by fish and chameleons. *Sci. Rep.* 6, 36557. <https://doi.org/10.1038/srep36557>.
22. Raut, H.K., Dinachali, S.S., Loke, Y.C., Ganesan, R., Ansah-Antwi, K.K., Góra, A., Khoo, E.H., Ganesh, V.A., Saifullah, M.S.M., and Ramakrishna, S. (2015). Multiscale ommatidial arrays with broadband and omnidirectional antireflection and antifogging properties by sacrificial layer mediated nanoimprinting. *ACS Nano* 9, 1305–1314. <https://doi.org/10.1021/nm505127z>.
23. Céspedes, E., Rodríguez-Palomo, A., Salas-Colera, E., Fonda, E., Jiménez-Villacorta, F., Vila, M., de Andrés, A., and Prieto, C. (2018). Role of  $\text{Al}_2\text{O}_3$  antireflective layer on the exceptional durability of Mo-Si-N-based spectrally selective coatings in air at high temperature. *ACS Appl. Energ. Mater.* 1, 6152–6160. <https://doi.org/10.1021/acsadm.8b01183>.
24. Hu, Z., Zhao, L., Jiang, T., Liu, J., Rashid, A., Sun, P., Wang, G., Yan, C., and Zhang, L. (2019). Trifluoropropylene carbonate-driven interface regulation enabling greatly enhanced lithium storage durability of silicon-based anodes. *Adv. Funct. Mater.* 29, 1906548. <https://doi.org/10.1002/adfm.201906548>.
25. Sakhuja, M., Son, J., Yang, H., Bhatia, C.S., and Danner, A.J. (2014). Outdoor performance and durability testing of antireflecting and self-cleaning glass for photovoltaic applications. *Sol. Energy* 110, 231–238. <https://doi.org/10.1016/j.solener.2014.07.003>.
26. Wang, C., Shi, J., Geng, Z., and Ling, X. (2016). Polychromic Al-AlN cermet solar absorber coating with high absorption efficiency and excellent durability. *Sol. Energy Mater. Sol. Cells* 144, 14–22. <https://doi.org/10.1016/j.solmat.2015.07.049>.
27. Yuan, Y., Chen, Y., Chen, W.L., and Hong, R.J. (2015). Preparation, durability and thermostability of hydrophobic antireflective coatings for solar glass covers. *Sol. Energy* 118, 222–231. <https://doi.org/10.1016/j.solener.2015.04.044>.
28. Luo, Z., Yu, T., Shang, J., Wang, Y., Lim, S., Liu, L., Gurzadyan, G.G., Shen, Z., and Lin, J. (2011). Large-scale synthesis of bi-layer graphene in strongly coupled stacking order. *Adv. Funct. Mater.* 21, 911–917. <https://doi.org/10.1002/adfm.201002227>.
29. Wang, S., Chen, F., Ji, R., Hou, M., Yi, F., Zheng, W., Zhang, T., and Lu, W. (2019). Ultrathin dielectric perfect absorber: large-area low-cost dielectric perfect absorber by one-step sputtering (advanced optical materials 9/2019). *Adv. Opt. Mater.* 7, 1970035. <https://doi.org/10.1002/adom.201970035>.
30. Wang, Z., Ding, H.L., Liu, D.L., Xu, C.H., Li, B., Niu, S.C., Li, J., Liu, L.P., Zhao, J., Zhang, J.Q., et al. (2021). Large-scale bio-inspired flexible antireflective film with scale-insensitivity arrays. *ACS Appl. Mater. Interfaces* 13, 23103–23112. <https://doi.org/10.1021/acsami.1c02046>.
31. Zheng, J., Mehrvarz, H., Liao, C., Bing, J., Cui, X., Li, Y., Gonçales, V.R., Lau, C.F.J., Lee, D.S., Li, Y., et al. (2019). Large-area 23%-efficient monolithic perovskite/homojunction-silicon tandem solar cell with enhanced UV stability using down-shifting material. *ACS Energy Lett.* 4, 2623–2631. <https://doi.org/10.1021/acsenergylett.9b01783>.
32. Jin, Y., Xu, W., Zhang, H., Zheng, H., Cheng, Y., Yan, X., Gao, S., Wang, D., Zi, Y., Zhou, F., and Wang, Z. (2021). Complete prevention of contact electrification by molecular engineering. *Matter* 4, 290–301. <https://doi.org/10.1016/j.matt.2020.10.019>.
33. Lv, M., Wang, Z., Jiao, C., Zhao, Y., Jin, L., Fu, Y., Liu, Q., and He, D. (2021). High-efficiency Si/PEDOT:PSS hybrid heterojunction solar cells using solution-processed graphene oxide as an antireflection and inversion-induced layer. *ACS Appl. Energ. Mater.* 4, 13279–13287. <https://doi.org/10.1021/acsadm.1c02869>.
34. Ralbag, N., Mann-Lahav, M., Davydova, E.S., Ash, U., Galed, R., Handl, M., Hiesgen, R., Magliocca, E., Mustain, W., He, J., et al. (2019). Composite materials with combined electronic and ionic properties. *Mater. Today* 1, 959–975. <https://doi.org/10.1016/j.matt.2019.04.007>.
35. Chen, R.Y., Lai, C.J., Chen, Y.J., Wu, M.X., and Yang, H. (2022). Omnidirectional/unidirectional antireflection-switchable structures inspired by dragonfly wings. *J. Colloid Interf. Sci.* 610, 246–257. <https://doi.org/10.1016/j.jcis.2021.12.025>.
36. Chien, C.Y., Chen, Y.H., Chen, R.Y., and Yang, H. (2019). Dragonfly-wing-inspired inclined irregular conical structures for broadband omnidirectional antireflection coatings. *ACS Appl. Nano Mater.* 3, 789–796. <https://doi.org/10.1021/acsanm.9b02301>.
37. Futahashi, R., Kawahara-Miki, R., Kinoshita, M., Yoshitake, K., Yajima, S., Arikawa, K., and Fukatsu, T. (2015). Extraordinary diversity of visual opsins genes in dragonflies. *Proc. Natl. Acad. Sci. U S A* 112, E1247–E1256. <https://doi.org/10.1073/pnas.1424670112>.
38. Kaya, M., Sargin, I., Al-Jaf, I., Erdogan, S., and Arslan, G. (2016). Characteristics of corneal lens chitin in dragonfly compound eyes. *Int. J. Biol. Macromol.* 89, 54–61. <https://doi.org/10.1016/j.ijbiomac.2016.04.056>.
39. Hänsler, M., Nádas, H., Feneberg, M., Marino, S., Giesselmann, F., Behrens, S., and Eremin, A. (2021). Magnetic tilting in nematic liquid crystals driven by self-assembly. *Adv. Funct. Mater.* 31, 2101847. <https://doi.org/10.1002/adfm.202101847>.
40. Li, T., Wang, B., Ning, J., Li, W., Guo, G., Han, D., Xue, B., Zou, J., Wu, G., Yang, Y., et al. (2019). Self-assembled nanoparticle supertubes as robust platform for revealing long-term, multiscale lithiation evolution. *Mater. Today* 1, 976–987. <https://doi.org/10.1016/j.matt.2019.04.009>.
41. Wang, Y., Mayyas, M., Yang, J., Tang, J., Ghasemian, M.B., Han, J., Elbourne, A., Daeneke, T., Kaner, R.B., and Kalantar-Zadeh, K. (2020). Self-deposition of 2D molybdenum sulfides on liquid metals. *Adv. Funct. Mater.* 31, 2005866. <https://doi.org/10.1002/adfm.202005866>.
42. Balzarotti, R., Cristiani, C., and Francis, L.F. (2017). Spin coating deposition on complex geometry substrates: influence of operative parameters. *Surf. Coat. Technol.* 330, 1–9. <https://doi.org/10.1016/j.surcoat.2017.09.077>.
43. Mali, S.S., Patil, J.V., Kim, H., Luque, R., and Hong, C.K. (2019). Highly efficient thermally stable perovskite solar cells via  $\text{Cs}_x\text{NiO}/\text{CuSCN}$  double-inorganic hole extraction layer interface engineering. *Mater. Today* 26, 8–18. <https://doi.org/10.1016/j.mattod.2019.01.017>.
44. Shen, S.J., Lee, D., Wu, Y.C., and Liu, S.J. (2021). Binary self-assembly of nanocolloidal arrays using concurrent and sequential spin coating techniques. *Materials* 14, 274. <https://doi.org/10.3390/ma14020274>.
45. Deng, S., and Berry, V. (2016). Wrinkled, rippled and crumpled graphene: an overview of formation mechanism, electronic properties, and applications. *Mater. Today* 19, 197–212. <https://doi.org/10.1016/j.mattod.2015.10.002>.
46. Feng, X., Surjadi, J.U., Fan, R., Li, X., Zhou, W., Zhao, S., and Lu, Y. (2021). Microalloyed medium-entropy alloy (MEA) composite nanolattices with ultrahigh toughness and cyclability. *Mater. Today* 42, 10–16. <https://doi.org/10.1016/j.mattod.2020.10.003>.
47. Shi, H., Chen, S., Shi, W., Peng, Z., Li, J., Liu, Z., Zhang, G., and Liu, L. (2021). High performance fiber-shaped supercapacitors based on core-shell fiber electrodes with adjustable surface wrinkles and robust interfaces. *J. Mater. Chem. 9*, 16852–16859. <https://doi.org/10.1039/dta04007c>.
48. Acharya, S., Yu, B.K., Hwang, J., Kim, J., and Kim, W. (2021). High thermoelectric performance of  $\text{ZnO}$  by coherent phonon scattering and optimized charge transport. *Adv. Funct. Mater.* 31, 2105008. <https://doi.org/10.1002/adfm.202105008>.
49. Chen, X., Liu, L., Feng, Y., Wang, L., Bian, Z., Li, H., and Wang, Z.L. (2017). Fluid eddy induced piezo-promoted photodegradation of organic dye pollutants in wastewater on  $\text{ZnO}$  nanorod arrays/3D Ni foam. *Mater. Today* 20,

- 501–506. <https://doi.org/10.1016/j.mattod.2017.08.027>.
50. Zhang, K., Chen, T., Abbas, Y., Jan, S.U., Zhou, Z., Chu, S., Xie, G., Ullah, S., Akram, M.Z., Zhang, J., et al. (2021). Atomic arrangement matters: band-gap variation in composition-tunable (Ga<sub>1-x</sub>Zn<sub>x</sub>)(N<sub>1-x</sub>O<sub>x</sub>) nanowires. *Matter* 4, 1054–1071. <https://doi.org/10.1016/j.matt.2020.12.024>.
51. Lan, W.X., Wang, Y.W., Singh, J., and Zhu, F.R. (2018). Omnidirectional and broadband light absorption enhancement in 2-D photonic-structured organic solar cells. *ACS Photonics* 5, 1144–1150. <https://doi.org/10.1021/acspophotonics.7b01573>.
52. Lan, W.X., Gu, J.L., Gao, X.H., Gong, C.L., Liu, Y.Y., Zhang, W.D., Sun, Y., Yue, T., Wei, B., and Zhu, F.R. (2022). Efficient and ultraviolet-durable nonfullerene organicsolar cells: from interfacial passivation and microstructural modification perspectives. *Adv. Mater. Interfaces* 9, 2101894. <https://doi.org/10.1002/admi.202101894>.
53. Lan, W.X., Gu, J.L., Wu, S.W., Peng, Y., Zhao, M., Liao, Y.J., Xu, T., Wei, B., Ding, L.M., and Zhu, F.R. (2021). Toward improved stability of nonfullerene organic solar cells: impact of interlayer and built-in potential. *EcoMat* 3, e12134. <https://doi.org/10.1002/eom2.12134>.
54. Hwang, I., Choi, D., Lee, S., Seo, J.H., Kim, K.H., Yoon, I., and Seo, K. (2017). Enhancement of light absorption in photovoltaic devices using textured polydimethylsiloxane stickers. *ACS Appl. Mater. Interfaces* 9, 21276–21282. <https://doi.org/10.1021/acsami.7b04525>.
55. Adhikari, S., Biswas, C., Doan, M.H., Kim, S.T., Kulshreshtha, C., and Lee, Y.H. (2019). Minimizing trap charge density towards an ideal diode in graphene–silicon Schottky solar cell. *ACS Appl. Mater. Interfaces* 11, 880–888. <https://doi.org/10.1021/acsami.8b18140>.
56. Bett, A.J., Winkler, K.M., Bivour, M., Cojocaru, L., Kabakli, O.Ş., Schulze, P.S.C., Siefer, G., Tutsch, L., Hermele, M., Glunz, S.W., and Goldschmidt, J.C. (2019). Semi-transparent perovskite solar cells with ITO directly sputtered on Spiro-OMeTAD for tandem applications. *ACS Appl. Mater. Interfaces* 11, 45796–45804. <https://doi.org/10.1021/acsami.9b17241>.